Original Article

Multiscale Simulation of Yield Strength in Reduced-Activation Ferritic/Martensitic Steel

Chenchong Wang [a], *Chi Zhang* [a,*], *Zhigang Yang* [a], *and Jijun Zhao* [b]

[a] *Key Laboratory of Advanced Materials of Ministry of Education, School of Materials Science and Engineering, Tsinghua University, No.1 Qinghua Yuan, North Zhongguancun Street, Beijing, China*
[b] *State Key Laboratory of Materials Modification by Laser, Electron, and Ion Beams, School of Physics and Optoelectronic Technology and College of Advanced Science and Technology, Dalian University of Technology, No.2, Linggong Street, Dalian, China*

ARTICLE INFO

ABSTRACT

One of the important requirements for the application of reduced-activation ferritic/martensitic (RAFM) steel is to retain proper mechanical properties under irradiation and high-temperature conditions. To simulate the yield strength and stress-strain curve of steels during high-temperature and irradiation conditions, a multiscale simulation method consisting of both microstructure and strengthening simulations was established. The simulation results of microstructure parameters were added to a superposition strengthening model, which consisted of constitutive models of different strengthening methods. Based on the simulation results, the strength contribution for different strengthening methods at both room temperature and high-temperature conditions was analyzed. The simulation results of the yield strength in irradiation and high-temperature conditions were mainly consistent with the experimental results. The optimal application field of this multiscale model was 9Cr series (7–9 wt.%Cr) RAFM steels in a condition characterized by 0.1–5 dpa (or 0 dpa) and a temperature range of 25–500°C.

Copyright © 2016, Published by Elsevier Korea LLC on behalf of Korean Nuclear Society. This is an open access article under the CC BY-NC-ND license (http://creativecommons.org/licenses/by-nc-nd/4.0/).

1. Introduction

One of the most important requirements of reduced-activation ferritic/martensitic (RAFM) steels is to retain proper mechanical properties in irradiation and high-temperature conditions [1–6]. However, testing the mechanical properties of materials under irradiation and high-temperature conditions is complicated and costly. To verify the accuracy of experimental results and to analyze the mechanisms associated with irradiation and high temperatures, much attention has been paid to simulations of the mechanical properties of RAFM steels under these conditions.

As a long-standing problem, yield strength simulations have been studied by many researchers, and many classical models have been established, including the Peierls–Nabarro (P–N) model [7,8], the Hall–Petch model [9,10], the Orowan dislocation looping model [11], Friedel's shear cutting model [12], and the Kocks–Mecking model [13–15]. Most of these models express one main strengthening method, with no

---

Please cite this article in press as: C. Wang et al., Multiscale Simulation of Yield Strength in Reduced-Activation Ferritic/Martensitic Steel, Nuclear Engineering and Technology (2016), http://dx.doi.org/10.1016/j.net.2016.10.006

relationships among them. To widen the application range of yield strength simulations, a superposition model [16], which combined different classical models, was built and used to calculate the yield strength of gear steels. However, this superposition model was only feasible for use under normal conditions (no irradiation at room temperature). In 2015, a self-consistent thermomechanical model was devised by Terentyev and co-workers [17] to simulate the strain-hardening behavior of polycrystalline tungsten at high temperatures. However, this model mainly expressed the effect of the temperature on dislocation strengthening without considering irradiation effects or other factors. Moreover, the Friedel–Kroupa–Hirsch model [12,18] and a dispersed barrier hardening model [19] have been widely used to calculate the irradiation effect on the yield strength of steels. However, these models only express factors related to He bubbles and dislocation loops [20].

In this work, a multiscale model, which consists of models at different scales and theories of different strength methods, is established to simulate the yield strength and stress-strain curve of RAFM steels in both irradiation and high-temperature conditions.

2. Simulation method

The applied model mainly consists of four strengthening models. Fig. 1 shows the overall simulation procedure of the proposed multiscale simulation model. To evaluate the accuracy and rationality of this model, it was used to analyze the effects of irradiation and high temperatures on the yield strength of F28H steel (Japanese RAFM steel tempered at 750°C for 1 h).

2.1. Microstructure simulation

2.1.1. Precipitation and solid solution
Thermodynamic theory is commonly used to simulate the volume fraction of precipitation, commonly using the Thermo-Calc software package (Thermo-Calc Software AB Company, Stockholm, Sweden) [21]. Previous work reported that the main precipitations that form in RAFM steels were MX, $M_{23}C_6$, and the Laves phase [22,23]. As $M_{23}C_6$ and the Laves phase typically form at the grain boundary and at much higher coarsening rates than the MX phase [23,24], the MX phase is regarded as the main reinforcement for dispersion strengthening. Fig. 2 shows the simulation results of the volume fraction of the MX phase and the concentration of the solid-solution element in the matrix of F28H steel.

2.1.2. Shear modulus
For steels, small changes in the atomic configuration triggered by temperature changes can change the magnetic interactions responsible for the nonrandom atomic spin orientation. In such a case, different magnetic states lead to different macroscopic properties, such as the shear modulus and elastic modulus [25,26]. Recently, many simulation results pertaining to ideal strength levels were obtained by first-principles methods. Based on these simulation results [25,27] and on experimental findings, a linear hypothesis was used to express the effect of the temperature on the shear modulus from 25°C to 500°C in RAFM steels, as shown in the following equation:

$$\mu = \mu_0 - k_{\text{shear}}\Delta T \tag{1}$$

where μ_0 is the shear modulus at 25°C and ΔT denotes the temperature increment.

2.1.3. He bubbles and dislocation loops
The formation of He bubbles and dislocation loops under an irradiation condition is a complicated problem that has been studied by many different simulation methods, including phase field theory, rate theory, and molecular dynamics [28–31]. A linear function passing through zero has been used to express the relationship between the irradiation and density/size of the dislocation loops. Based on both simulation and experimental results, a linear hypothesis has been used to express the effects of accumulated displacement damage on
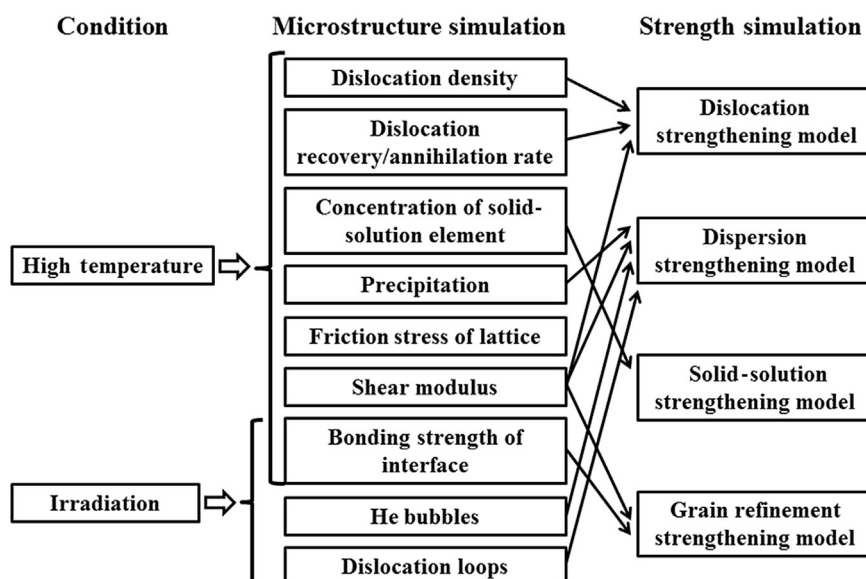

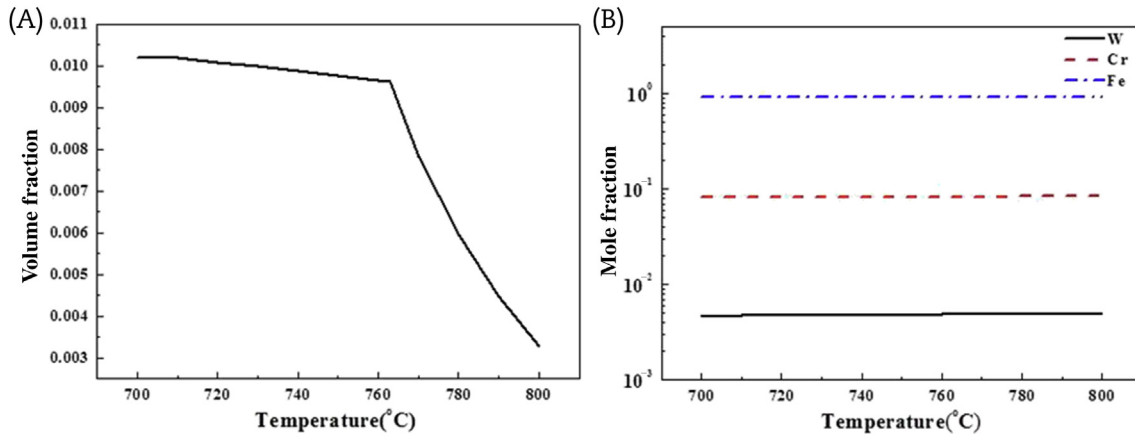**Fig. 1 – Simulation procedure of the multiscale simulation model.**

Fig. 2 – Simulation results of volume fraction of the MX phase and concentration of solid-solution element in the matrix of F28H steel. (A) Volume fraction of the MX phase; (B) concentration of the solid-solution element.

the density/size of He bubbles at the growth stage from 0.1 dpa to 5 dpa in RAFM steels, as shown in Eqs. (2) and (3) [32–34].

$$d_H = d_0 + k_{d-He}\Delta\phi \tag{2}$$

$$N_H = N_0 + k_{N-He}\Delta\phi \tag{3}$$

In these equations, d_0 and N_0 denote the initial diameter and the density of He bubbles at 0.1 dpa, respectively, and $\Delta\phi$ is the accumulated displacement damage increment. Except for these factors, other information about the microstructure included in Fig. 1 was not a key factor. Therefore, only these values are listed as parameters in Section 3.

2.2. Strengthening simulation

2.2.1. Kocks–Mecking model
The stress-strain curve can be divided to three parts: the elastic stage ($\varepsilon < \varepsilon_I$), the homogeneous plastic deformation stage ($\varepsilon_I \leq \varepsilon < \varepsilon_{II}$), and the inhomogeneous plastic deformation stage ($\varepsilon \geq \varepsilon_{III}$). The modified Kocks–Mecking model was used to simulate dislocation strengthening [15], as expressed by Eqs. (4–6):

$$\frac{d\rho}{d\varepsilon} = \begin{cases} 0 & \varepsilon < \varepsilon_I \\ k_1\sqrt{\rho(T,\varepsilon)} - k_2(T)\rho(T,\varepsilon) & \varepsilon_I \leq \varepsilon < \varepsilon_{II} \\ k_1\sqrt{\rho(T,\varepsilon)}\exp[-\xi(T)\sqrt{\rho(T,\varepsilon}] & \varepsilon \geq \varepsilon_{II} \end{cases} \tag{4}$$

$$k_2 = \chi\frac{k_1 b}{E_a}\left[1 - \frac{k_B T}{cb^3}\ln\left(\frac{\dot{\varepsilon}}{\dot{\varepsilon}_0}\right)\right] \tag{5}$$

$$\xi = \delta \cdot k_2^n \tag{6}$$

where k_1 is the Kocks–Mecking parameter, χ is the interaction parameter, E_a represents the normalized activation energy, c is the proportionality constant, $\dot{\varepsilon}$ represents the mean shear rate, $\dot{\varepsilon}_0$ denotes the reference shear rate, δ is the annihilation parameter for the inhomogeneous plastic deformation stage, and n is the index parameter.

The shear stress of dislocation strengthening is expressed as follows:

$$\tau_d = \alpha\mu(T)b\sqrt{h_d(T)\rho} \tag{7}$$

where α is a constant of order unity, which depends on the strength of the dislocation/dislocation interaction and h_d denotes the dislocation–dislocation interaction strength, which is expressed as follows:

$$h_d = \begin{cases} a_{1h} + k_{1h}T & T \leq T_c \\ a_{2h} + k_{2h}T & T > T_c \end{cases} \tag{8}$$

where T_c is the critical temperature based on the temperature-dependent dislocation–dislocation interaction theory [17].

2.2.2. Hall–Petch model
For grain refinement strengthening, the Hall–Petch stress is given by Eqs. (9) and (10) [35–38]:

$$\sigma_{H-P} = \sigma_0 + K_{H-P}d^{1/2} \tag{9}$$

$$K_{H-P} = K_0 + k_{irr}\phi + k_T\exp(a_T\Delta T) \tag{10}$$

where σ_0 is the P–N stress, K_{H-P} is the Hall–Petch constant, and d is the martensite packet size. A high temperature would decrease the bonding strength of the grain boundary directly, but the precipitation formed at the grain boundary ($M_{23}C_6$, Laves phase) would also pin the grain boundary and enhance the bonding strength. Consequently, the value of K_{H-P} can be expressed by Eq. (10).

According to the P–N model [8] and to Lim's model [35], the P–N stress can be expressed by Eqs. (11) and (12):

$$\sigma_0 = \sigma_f\left[1 - \frac{k_B T\ln\left(\dot{\gamma}_p/\dot{\varepsilon}\right)}{2H_k}\right]^2 \tag{11}$$

$$\sigma_f = M\frac{\mu(T)}{1-\nu}\exp\left[-\frac{2\pi d_s}{b(1-\nu)}\right] \tag{12}$$

where $\dot{\gamma}_p$ is the reference strain rate, H_k denotes the double-kink activation enthalpy, d_s is the spacing of the slip planes, ν is Poisson's ratio, and M represents the Taylor factor for RAFM steels.

2.2.3. Orowan bypass model
Previous studies on microstructural observations in RAFM steels showed that the diameter of the MX phase is much

larger than the critical value of coherence [22,23]. Only an equilibrium content was used in the simulations of the precipitate and element distributions, as the contents of the precipitates and elements nearly reached a state of equilibrium, as proved in previous experimental results [22,23]. A modified Orowan bypass model was used to express dispersion strengthening, as shown in Eqs. (13–16):

$$\tau_p = Y\frac{2Kb}{w_L\overline{R}}\ln\left(\frac{2w_D\overline{R}}{b}\right)\sqrt{\frac{\ln\left(\frac{2w_D\overline{R}}{b}\right)}{\ln\left(\frac{w_L\overline{R}}{b}\right)}} \qquad (13)$$

$$w_L = \sqrt{\frac{\pi w_q}{\varphi_{MX}}} - 2w_r \qquad (14)$$

$$w_D = \left(\frac{1}{w_L} + \frac{1}{2w_r}\right)^{-1} \qquad (15)$$

$$K = \frac{\mu(T)}{4\pi}\sqrt{\frac{1}{1-\nu}} \qquad (16)$$

where Y represents the precipitate spatial-distribution parameter for Orowan dislocation looping; w_r and w_q represent the mean radius and the mean area of the particle intersection with the glide plane, respectively; ν is Poisson's ratio; and φ_{MX} and $\overline{R}$ are the volume fraction and mean radius of the MX phase, respectively.

2.2.4. Solid-solution model

The solid-solution strengthening of RAFM steels was calculated using the following equation:

$$\tau_{ss} = \left(\sum_i k_{ss,i}^2 c_i\right)^{1/2} \qquad (17)$$

where $k_{ss,i}$ is the strengthening coefficient of element i in the matrix. In addition, c_i is the atomic fraction of element i in the matrix.

2.2.5. Yield strength model

A superposition equation was established to combine all of these strengthening constituents using Eq. (18).

$$\sigma_s = M\left[\tau_d + \left(\tau_{ss}^k + \tau_p^k\right)^{\frac{1}{k}}\right] + \sigma_{H-P} + \Delta\sigma_{irr} \qquad (18)$$

According to the Friedel–Kroupa–Hirsch model [12] and the dispersed barrier hardening model [19], $\Delta\sigma_{irr}$ can be expressed as follows:

$$\Delta\sigma_{irr}(T,\phi) = \alpha M\mu(T)b\sqrt{N_{dl}(\phi)\overline{d}_{dl}(\phi)} + \beta M\mu(T)bd_H(\phi)N_H(\phi)^{2/3} \qquad (19)$$

3. Results and discussion

Fig. 3 shows the simulation results of the stress-strain curve and yield strength with an increase in the temperature. The stress–strain curve shows a trend identical to those in other simulations in previous works [17,39]. The simulation results of the yield strength were essentially consistent with earlier experimental results [40]. Table 1 presents the simulation results of the strength contribution for different strengthening methods. At room temperature, the P–N stress and grain refinement collectively account for a relatively large proportion. The solid-solution strengthening was scarcely changed by the temperature; therefore, its absolute value remains constant and the percentage increases with an increase in the temperature.

Fig. 4 shows the simulation results of the effects of irradiation and temperature on the yield strength. The simulation results were mainly consistent with earlier experimental results [41,42]. Table 2 presents all of the parameters used in the model. The values of most parameters (61%) were obtained through simulations using thermodynamic, first-principles, phase field, rate theory, or other constitutive models. However, the values of parameters that could not be calculated accurately by any simulation method were obtained from experiment results (21%) or through fitting (18%). Accordingly, this model remains not perfectly suitable as a widely predictive model for every type of steel, at least until the parameters obtained from experimental results or fittings can be calculated accurately by simulation methods. For 9Cr series (7–9 wt.%Cr) RAFM steels with the condition of 0.1–5 dpa (or
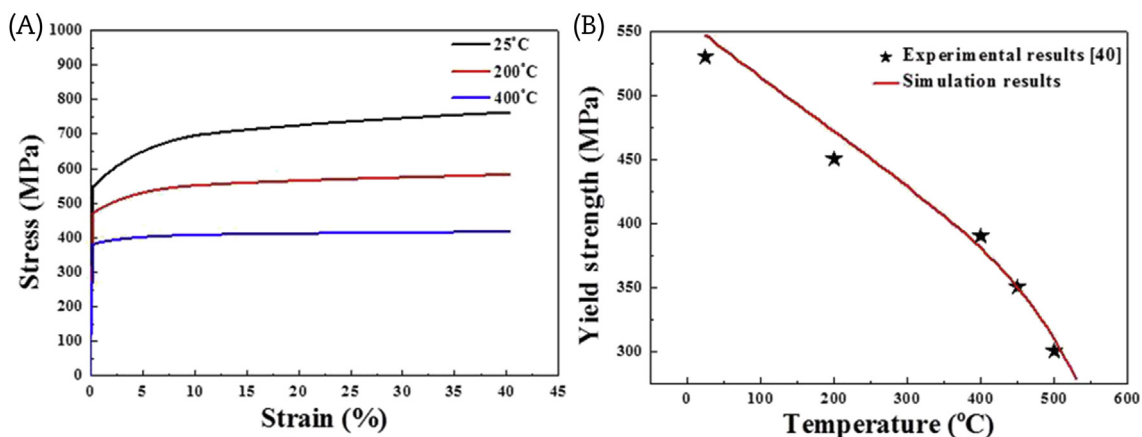

Fig. 3 – Simulation results of stress-strain curve and yield strength with the increase of temperature in the condition of 0 dpa. (A) Stress-strain curve; (B) yield strength.

Table 1 – Simulation results of strength contribution for different strengthening methods.

Strengthening constituents	P–N	Grain refinement	Solid solution	Dispersion	Dislocation
Strength fraction at 25°C, %	45	22	19	10	4
Strength fraction at 500°C, %	36	15	34	12	3
Strength change from 25°C to 500°C, MPa	−135	−76	−1	−15	−10

P–N, Peierls–Nabarro.
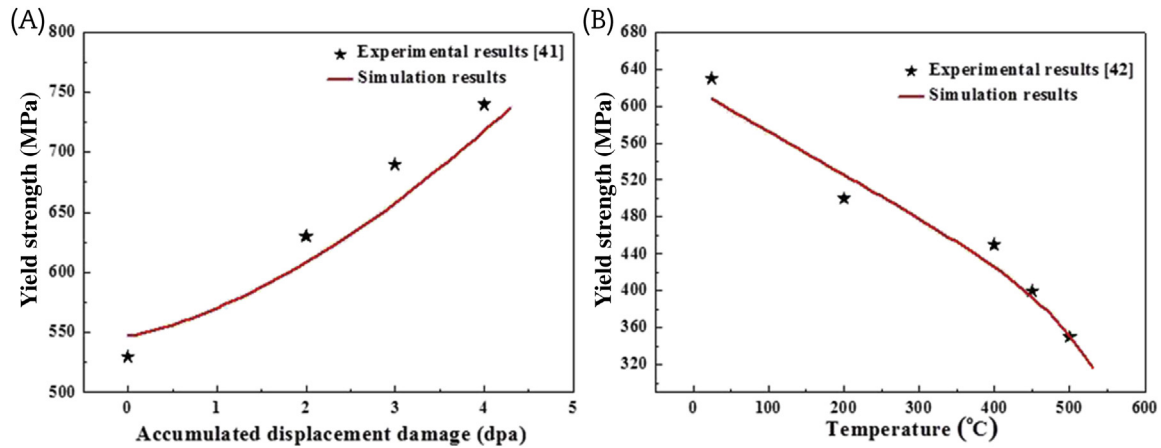
Fig. 4 – Simulation results of the effect of irradiation and temperature on yield strength. (A) Effect of irradiation in the condition of 25°C; (B) effect of temperature in the condition of 2 dpa.

0 dpa) and 25–500°C, the difference between simulation results and experimental results for the yield strength was found to be approximately ± 30 MPa, which is an acceptable error range. For extremely high temperatures (>500°C), the

Table 2 – Parameters used in the simulation procedure.

Parameter	Value	Parameter	Value
μ_0	77 GPa[a]	c	10^{11}[b]
k_{shear}	5.37×10^7 Pa/K[c]	$\dot{\varepsilon}$	10^{-3} 1/s[a]
d_0	0.02 nm[c]	$\dot{\varepsilon}_0$	10^7 1/s[a]
$k_{d\text{-}He}$	0.2 nm/dpa[a]	δ	2.5×10^{-9}[c]
N_0	1×10^{22} 1/m³[a]	n	1.3[b]
$K_{N\text{-}He}$	1×10^{23} 1/(m³·dpa)[c]	α	0.4[b]
ρ_0	5×10^{12} 1/m³[a]	k_{2h}	4×10^{-4}[c]
k_B	1.38×10^{-23}[c]	a_{2h}	0.38[c]
b	0.248 nm[c]	$\dot{\gamma}_p$	3.71×10^{10} 1/s[a]
D_c	7×10^{-8} m/s[c]	H_k	1.65×10^{-19} J[c]
C	10^{-10}[c]	ν	0.3[c]
k_1	3.73×10^{-8} 1/m[b]	M	2.5[c]
χ	0.9[c]	k_{irr}	200[b]
E_a	3.8×10^{-3}[b]	k_T	3×10^3[b]
Y	0.65[c]	a_T	0.01[b]
w_r	0.82[c]	β	0.7[c]
w_q	0.75[c]	N_{dl}	1×10^{19} 1/m³[a]
T_c	473 K[c]	k	1.8[c]
φ_{MX}	0.01[c]	d_{dl}	100 nm[c]
$\overline{R}$	25 nm[a]	$k_{ss,Cr}$	82.7 MPa[c]

[a] Obtained from experiment results in references [3,5,16–18,23,26,40].
[b] Obtained from fitting.
[c] Obtained from simulation results or classical constant [7,8,10–13,15,25,29–33,35,37].

bonding strength of the grain boundary would decrease significantly. As a result, the decrease in the Hall–Petch constant would deviate from the hypothesis model in Eq. (10) when the temperature reaches 500°C. This would lead to additional error and inaccuracies in this model. As determining the interaction between the temperature and irradiation is too complicated in this model, the temperature and irradiation are regarded as two separate factors. This explains why the error in the simulation would be significant under high-temperature and high-irradiation conditions. When the accumulated displacement damage reaches 0.1 dpa, the density/size of the dislocation loops can be assumed to be constant and the density/size of the He bubbles can be assumed to follow a linear function. However, at 0–0.1 dpa, the growth of both dislocation loops and He bubbles shows a long incubation stage, very different from a constant or linear growth stage. As a result, additional errors would also be included in the models owing to the inaccurate expressions of the growth processes of dislocation loops and He bubbles.

4. Conclusion

The dispersion and solid-solution parameters were calculated by thermodynamic theory. Dislocation loops and He bubbles were also expressed according to previous results, which relied on phase field and rate theory. The simulation results of microstructural parameters were added to a superposition strengthening model. The simulation results showed that the P–N stress and grain refinement accounted for relatively large proportions of the strength and that solid-solution strengthening was scarcely changed by temperature changes. All of

the simulation results of the yield strength under irradiation and high-temperature conditions were generally consistent with earlier experimental results. The optimal application field of this multiscale model was as follows: 9Cr series (7–9 wt.%Cr) RAFM steels with the condition of 0.1–5 dpa (or 0 dpa) and 25–500°C.

Conflicts of interest

The authors have no conflicts of interest.

Acknowledgments

REFERENCES

[1] Z.X. Xia, C. Zhang, H. Lan, Z.Q. Liu, Z.G. Yang, Effect of magnetic field on interfacial energy and precipitation behavior of carbides in reduced activation steels, Mater. Lett. 65 (2011) 937–939.

[2] M.N. Babu, G. Sasikala, B.S. Dutt, S. Venugopal, A.K. Bhaduri, T. Jayakumar, Fatigue crack growth behavior of RAFM steel in Paris and threshold regimes at different temperatures, Nucl. Eng. Des. 269 (2014) 103–107.

[3] W. Wang, S. Liu, G. Xu, B. Zhang, Q. Huang, Effect of thermal aging on microstructure and mechanical properties of China low-activation martensitic steel at 550°C, Nucl. Eng. Technol. 48 (2016) 518–524.

[4] T.K. Kim, S. Noh, S.H. Kang, J.J. Park, H.J. Jin, M.K. Lee, J. Jang, C.K. Rhee, Current status and future prospective of advanced radiation resistant oxide dispersion strengthened steel (ARROS) development for nuclear reactor system applications, Nucl. Eng. Technol. 48 (2016) 572–594.

[5] L. Huang, X. Hu, W. Yan, W. Sha, F. Xiao, Y. Shan, K. Yang, Laves-phase in the China low activation martensitic steel after long-term creep exposure, Mater. Des. 63 (2014) 333–335.

[6] W.B. Liu, C. Zhang, Z.X. Xia, Z.G. Yang, P.H. Wang, J.M. Chen, Strain-induced refinement and thermal stability of a nanocrystalline steel produced by surface mechanical attrition treatment, Mater. Sci. Eng. A 568 (2013) 176–183.

[7] G.F. Wang, A. Strachan, C. Tahir, W.A. Goddard, Calculating the Peierls energy and Peierls stress from atomistic simulations of screw dislocation dynamics: application to bcc tantalum, Model. Simul. Mat. Sci. Eng. 12 (2004) S371–S389.

[8] F.R.N. Nabarro, Fifty-year study of the Peierls–Nabarro stress, Mater. Sci. Eng. A 234–236 (1997) 67–76.

[9] Y.Z. Zhu, S.Z. Wang, B.L. Li, Z.M. Yin, Q. Wan, P. Liu, Grain growth and microstructure evolution based mechanical property predicted by a modified Hall-Petch equation in hot worked Ni76Cr19AlTiCo alloy, Mater. Des. 55 (2014) 456–462.

[10] N. Hansen, Hall-Petch relation and boundary strengthening, Scr. Mater. 51 (2004) 801–806.

[11] M.F. Ashby, On the Orowan Stress, MIT Press, Cambridge, MA, 1969.

[12] J. Friedel, Dislocations, Pergamon Press, New York, 1964.

[13] H. Meckings, U.F. Kocks, Kinetics of flow and strain-hardening, Acta Metallurgica 29 (1981) 1865–1875.

[14] J. Kang, T. Ingendahl, W. Bleck, A constitutive model for the tensile behaviour of TWIP steels: composition and temperature dependencies, Mater. Des. 90 (2016) 340–349.

[15] O. Bouaziz, Revised storage and dynamic recovery of dislocation density evolution law: toward a generalized Kocks–Mecking model of strain-hardening, Adv. Eng. Mater. 14 (2012) 759–761.

[16] J.S. Wang, M.D. Mulholland, G.B. Olson, D.N. Seidman, Prediction of the yield strength of a secondary-hardening steel, Acta Mater. 61 (2013) 4939–4952.

[17] D. Terentyev, X. Xiao, A. Dubinko, A. Bakaeva, H. Duan, Dislocation-mediated strain hardening in tungsten: thermo-mechanical plasticity theory and experimental validation, J. Mech. Phys. Solids 85 (2015) 1–15.

[18] S.J. Zinkle, Y. Matsukawa, Observation and analysis of defect cluster production and interactions with dislocations, J. Nucl. Mater. 329–333 (2004) 88–96.

[19] A.K. Seeger, On the theory of radiation damage and radiation hardening, Second UN Conference on Peaceful Uses of Atomic Energy, United Nations, New York, 1958.

[20] C. Wang, C. Zhang, Z. Yang, J. Su, Y. Weng, Multi-scale simulation of hydrogen influenced critical stress intensity in high Co-Ni secondary hardening steel, Mater. Des. 87 (2015) 501–506.

[21] C. Wang, C. Zhang, Z. Yang, Austenite layer and precipitation in high Co-Ni maraging steel, Micron 67 (2014) 112–116.

[22] P.P. Liu, M.Z. Zhao, Y.M. Zhu, J.W. Bai, F.R. Wan, Q. Zhan, Effects of carbide precipitate on the mechanical properties and irradiation behavior of the low activation martensitic steel, J. Alloys Compd. 579 (2013) 599–605.

[23] R. Schaublin, P. Spatig, M. Victoria, Microstructure assessment of the low activation ferritic/martensitic steel F82H, J. Nucl. Mater. 258 (1998) 1178–1182.

[24] K.W. Tupholme, D. Dulieu, G.J. Butterworth, The effect of aging on the properties and structures of low activation martensitic 9 and 11-percent Cr, W, V stainless-steel, J. Nucl. Mater. 179 (1991) 684–688.

[25] X. Li, S. Schönecker, E. Simon, L. Bergqvist, H. Zhang, L. Szunyogh, J. Zhao, B. Johansson, L. Vitos, Tensile strain-induced softening of iron at high temperature, Sci. Rep. 5 (2015) 16654.

[26] R. Lowrie, A.M. Gonas, Single-crystal elastic properties of tungsten from 24 degree to 1800 degree, J. Appl. Phys. 38 (1967) 4505.

[27] S.L. Shang, W.Y. Wang, Y. Wang, Y. Du, J.X. Zhang, A.D. Patel, Z.K. Liu, Temperature-dependent ideal strength and stacking fault energy of fcc Ni: a first-principles study of shear deformation, J. Phys. Condens. Matter. 24 (2012) 155402.

[28] C.W. Lee, A. Chernatynskiy, P. Shukla, R.E. Stoller, S.B. Sinnott, S.R. Phillpot, Effect of pores and He bubbles on the thermal transport properties of UO_2 by molecular dynamics simulation, J. Nucl. Mater. 456 (2015) 253–259.

[29] Y. Watanabe, K. Morishita, T. Nakasuji, M. Ando, H. Tanigawa, Helium effects on microstructural change in RAFM steel under irradiation: reaction rate theory modeling, Nucl. Instrum. Methods Phys. Res. B 352 (2015) 115–120.

[30] Y. Li, S. Hu, R. Montgomery, F. Gao, X. Sun, Phase-field simulations of intragranular fission gas bubble evolution in UO_2 under post-irradiation thermal annealing, Nucl. Instrum. Methods Phys. Res. B 303 (2013) 62–67.

[31] Y. Yu, X. He, F. Luo, L. Guo, Rate theory modeling of dislocation loops in RAFM steel under helium ion irradiation and comparison with experiments, Comp. Mater. Sci. 110 (2015) 34–38.

[32] P.C. Millett, M. Tonks, Phase-field simulations of gas density within bubbles in metals under irradiation, Comp. Mater. Sci. 50 (2011) 2044—2050.

[33] A. Abhishek, M. Warrier, R. Ganesh, A. Caro, Growth and structural determination of He bubbles in iron/chromium alloys using molecular dynamics simulations, J. Nucl. Mater. 472 (2016) 82—88.

[34] E. Nes, Recovery revisited, Acta Metall. Mater. 43 (1995) 2189—2207.

[35] H. Lim, C.C. Battaile, J.D. Carroll, B.L. Boyce, C.R. Weinberger, A physically based model of temperature and strain rate dependent yield in BCC metals: implementation into crystal plasticity, J. Mech. Phys. Solids 74 (2015) 80—96.

[36] A. Dunn, R. Dingreville, E. Martínez, L. Capolungo, Identification of dominant damage accumulation processes at grain boundaries during irradiation in nanocrystalline α-Fe: a statistical study, Acta Mater. 110 (2016) 306—323.

[37] N. Ono, R. Nowak, S. Miura, Effect of deformation temperature on Hall-Petch relationship registered for polycrystalline magnesium, Mater. Lett. 58 (2004) 39—43.

[38] K.L. Murty, Role and significance of source hardening in radiation embrittlement of iron and ferritic steels, J. Nucl. Mater. 270 (1999) 115—128.

[39] E. Shafiei, High strain rate behavior of alloy 800H at high temperatures, J. Nucl. Mater. 473 (2016) 1—5.

[40] R.J. Kurtz, A. Alamo, E. Lucon, Q. Huang, S. Jitsukawa, A. Kimura, R.L. Klueh, G.R. Odette, C. Petersen, M.A. Sokolov, P. Spätig, J.W. Rensman, Recent progress toward development of reduced activation ferritic/martensitic steels for fusion structural applications, J. Nucl. Mater. 386—388 (2009) 411—417.

[41] N.M. Ghoniem, G. Po, S. Sharafat, Deformation mechanisms in ferritic/martensitic steels and the impact on mechanical design, J. Nucl. Mater. 441 (2013) 704—712.

[42] E. Wakai, M. Ando, T. Sawai, H. Tanigawa, T. Taguchi, R.E. Stoller, T. Yamamoto, Y. Kato, F. Takada, Effect of heat treatments on tensile properties of F82H steel irradiated by neutrons, J. Nucl. Mater. 367—370 (2007) 74—80.